Published in final edited form as:
IEEE Trans Biomed Eng. 2012 April ; 59(4): 936–945. doi:10.1109/TBME.2011.2176727.

A TSVD Analysis of Microwave Inverse Scattering for Breast Imaging

Jacob D. Shea[*] **[Member, IEEE]**, **Barry D. Van Veen [Fellow, IEEE]**, and **Susan C. Hagness [Fellow, IEEE]**
Department of Electrical and Computer Engineering, University of Wisconsin-Madison, Madison, WI 53706 USA (vanveen@engr.wisc.edu; hagness@engr.wisc.edu)

Abstract

A variety of methods have been applied to the inverse scattering problem for breast imaging at microwave frequencies. While many techniques have been leveraged toward a microwave imaging solution, they are all fundamentally dependent on the quality of the scattering data. Evaluating and optimizing the information contained in the data are, therefore, instrumental in understanding and achieving optimal performance from any particular imaging method. In this paper, a method of analysis is employed for the evaluation of the information contained in simulated scattering data from a known dielectric profile. The method estimates optimal imaging performance by mapping the data through the inverse of the scattering system. The inverse is computed by truncated singular-value decomposition of a system of scattering equations. The equations are made linear by use of the exact total fields in the imaging volume, which are available in the computational domain. The analysis is applied to anatomically realistic numerical breast phantoms. The utility of the method is demonstrated for a given imaging system through the analysis of various considerations in system design and problem formulation. The method offers an avenue for decoupling the problem of data selection from the problem of image formation from that data.

Index Terms

Biomedical imaging; eigenvalues and eigenfunctions; inverse problems; microwave imaging

I. Introduction

Research into the use of microwaves for medical imaging has focused on breast imaging, as the location exterior to the high-loss thoracic wall and the low-loss adipose tissue content of the breast make the measurement of scattered waves feasible [1]. In addition, the dielectric contrast at microwave frequencies between the constituent tissue types of the breast [2] provides an electromagnetic mechanism for sensing, locating, and identifying tissue structure. However, substantial technical challenges remain due in part to the relatively low

[*]Department of Electrical and Computer Engineering, University of Wisconsin-Madison, Madison, WI 53706 USA (jacob_shea@ieee.org).

Color versions of one or more of the figures in this paper are available online at http://ieeexplore.ieee.org.

Authors' photographs and biographies not available at the time of publication.

resolution of microwaves and indications of modest contrast between normal and malignant tissues [3].

Inverse scattering techniques provide a quantitative estimation of a spatial profile of dielectric properties over an imaging region [4] and can account for the scattering responses of both malignant and healthy fibroglandular tissue structures—both of which have high contrast against a background of adipose tissue. However, inverse scattering systems for breast imaging are often designed for frequencies in the UHF band (0.3 to 3 GHz), since signal to noise levels and inverse solution efficiencies tend to become more onerous at higher microwave frequencies. The longer wavelengths of the UHF band scatter less efficiently from the millimeter-scale fine details of the connective, ductal, and glandular tissue structures in the breast. The resulting loss of imaging resolution has led to the investigation of techniques and algorithms capable of overcoming the nonlinearity of the scattering while improving image resolution and preserving the boundaries between adjacent tissue types (see, e.g., [5]–[9]).

While there is a considerable amount of contemporary research into imaging techniques that can be used to reconstruct the breast profile from the scattering data (see, e.g., [10]–[15]), there is comparatively little qualification of the data itself. The information available from the data is typically considered only indirectly by the evaluation of a final image that is obscured by unrelated uncertainties and errors. Such evaluations need not be made indirectly, as there are two relatively distinct technical components to the microwave imaging problem. The first is the design of the measurements and the formulation of the inverse problem from the resulting data; the second is the selection and development of an imaging method to efficiently and accurately image the breast from that data. It is natural, then, to decouple these two components to ensure that the success of an imaging algorithm is not hindered by poor choices in data selection or problem formulation.

Many prior contributions have considered the fundamental limitations of scattering data in the reconstruction of an unknown object or source profile. Slaney *et al.* [16] showed the limitations of the Born and Rytov field approximations in microwave tomography. Bucci and Franceschetti [17], [18] studied the degrees of freedom and band-limitation of scattered fields with finite measurement precision and investigated the maximum number of recoverable unknowns for radiative-region scattered field observations [19]. Hori [20] presented an analysis method for geophysical inverse problems in which Green's function is spectrally decomposed and the inverse problem is evaluated by a truncated set of eigenfunctions. The use of singular-value decomposition (SVD) in the evaluation of ill-posed inverse problems is described in detail by Hansen [21]. Singular-value analysis has been used previously in the study of microwave imaging. Fang *et al.* [22] used SVD to evaluate the effect of various design parameters on the invertibility of the microwave imaging problem. The study was limited to a 2-D background region for which the singular spectrum of the scattering matrix was used to compare the degree of ill posedness of the inverse problem as a parameter of interest was varied. Winters *et al.* [23] used SVD to create a custom spatial basis for the solution that was preregularized to remove basis functions that would not be resolved by the illumination. Crocco and Litman [24] studied the information

available in a metal-encased imaging apparatus by evaluating the SVD of the scattering operator.

In this paper, we apply a truncated SVD (TSVD) method of analysis in order to decouple the obfuscating issues arising in the solution of nonlinear inverse problems from the evaluation of the quality of the scattering data with respect to system design and problem formulation. The nonlinearity of the problem is avoided by making use of *a priori* knowledge of the exact fields over the object region. The problem is then linearized without resorting to field approximation. The exact fields are readily available from electromagnetic simulations when studying test objects in a purely computational environment. Our MRI-derived, 3-D numerical breast phantoms [25], [26], therefore, offer ideal test cases for the analysis. These high-fidelity numerical phantoms are realistic in tissue distribution and incorporate dielectric properties data from a thorough study on the microwave properties of normal breast tissue, allowing for the simulated acquisition of realistic data. We compute the vector fields and tensor Green's functions for the breast phantoms using finite-difference time-domain (FDTD) simulations. The imaging region is illuminated by electrically short current sources for each orthogonal linear polarization. A system of scattering equations is constructed and then evaluated using the controlled regularization of the TSVD inversion. The TSVD analysis provides a systematic investigation of the quality and quantity of information contained in the scattering data and the performance relative to various system design considerations. Specifically, we investigate single-frequency formulations, multiple-frequency formulations, approximated-field formulations, channel selection, and noise performance. The method provides both an illustration and quantification of the potential imaging performance for a given scenario. Comparative results may be used as a guide in the design of the measurement system and formulation of the inverse problem. Projected images from the TSVD analysis may be used as a reference for evaluating practical imaging performance.

In the next section, we provide a brief background for electromagnetic inverse scattering and TSVD analysis. In Section III, the details of the analysis are presented in the context of the microwave breast imaging problem. The test phantoms are presented in Section IV, and in Section V, the analysis is applied to the phantoms. A discussion of the analysis and the results follows in Section VI and the investigation is concluded in Section VII.

II. Background

We focus our attention in this investigation to breast imaging using methods of electromagnetic inverse scattering. In general, inverse scattering techniques reconstruct an estimate of the dielectric properties of an unknown object by inverting a system of equations describing electromagnetic scattering in the presence of an unknown object. In this section, we briefly review the object–scattering relationship and the general form of the inverse problem.

Let an imaging target in a known background of complex wavenumber k_b be described by an unknown spatial distribution, over a finite volume V, of the complex wavenumber $k(r)$ where r is a position vector. Let $\boldsymbol{E}^b$ be the incident field over V in a known background, let

$\boldsymbol{E}^t$ be the total field in V in the presence of the object to be imaged, and define the scattered field as $\boldsymbol{E}^s = \boldsymbol{E}^t - \boldsymbol{E}^b$. Given a tensor Green's function solution for the background profile $\overline{\boldsymbol{G}^b}$ a frequency domain integral equation is available to express the electromagnetic scattering from an object, due to a source at r_{src} and observed at r_{obs}, in terms of the unknown wavenumber contrast

$$\boldsymbol{E}^s(\boldsymbol{r}_{\mathrm{obs}}, \boldsymbol{r}_{\mathrm{src}}) = \int_V \overline{\boldsymbol{G}}^b(\boldsymbol{r}_{\mathrm{obs}}, \boldsymbol{r}')\boldsymbol{E}^t(\boldsymbol{r}', \boldsymbol{r}_{\mathrm{src}})(k^2(\boldsymbol{r}') - k_b^2(\boldsymbol{r}'))d\boldsymbol{r}'. \quad (1)$$

The electromagnetic scattering relationship is notably characterized by its nonlinearity due to the dependence of the total field $\boldsymbol{E}^t$ on the unknown object profile $k(\boldsymbol{r})$. In this paper, we avoid the nonlinearity by exploiting the computational availability of exact total fields.

The scattering data $\boldsymbol{E}^s$ are the difference between measurements of the total field and measurements or computations of the background field. Measurements are collected over a set of spatial channels (selections of source and observation point pairs) and over a set of frequency channels (selections of source frequencies), resulting in a system of equations in the unknown wavenumber, in which each equation is formed as in (1). Since continuous closed-form inverse operators are unavailable for the general scattering problem, the scattering equations are typically discretized over a finite spatial basis, yielding a system of linear equations composed of an $M \times N$ scattering matrix $\mathbf{A}$ an $N \times 1$ vector x of the unknown contrast function, and an $M \times 1$ a vector of scattered field data $\mathbf{b}$. In the basic formulation, M is the number of channel measurements and N is the number of spatial basis functions in the discretization. While the selection of field data, the choice of unknown parameters, and use of simplifying assumptions may vary, we will refer to any particular formulation of the linear problem in the generic form $\mathbf{Ax} = \mathbf{b}$.

Both linear and nonlinear inverse problems are often posed as a minimization of a cost function having the general form

$$\min_{\mathrm{x}}\{\|\mathbf{Ax} - \mathbf{b}\| + \lambda \mathbf{p}(\mathrm{x})\} \quad (2)$$

where the residual error $\mathbf{Ax} - \mathbf{b}$ is minimized over a selected norm and a penalization term p(x) is added or multiplied (cf. [7] and references therein) in an amount controlled by a tuning parameter λ to encourage or discourage certain solutions based on *a priori* assumptions about desirable solution characteristics. The residual term represents the phenomenological cost (i.e., how well the the scattering model and the estimate of the object predict the physical scattering phenomena of the true object), while the penalization term represents the presumptive cost (i.e., how well the estimate of the object agrees with known features of the true object).

In this paper, we are specifically interested in comparatively evaluating the phenomenological cost of the problem, since higher quality images will result from any approach to the solution of (2) which operates on superior data. We wish to evaluate the information available from the scattering data $\mathbf{b}$ and the ability of the formulation of $\mathbf{A}$ to

estimate the unknown object from the data. To this end, we employ the singular-value decomposition of the scattering matrix. The SVD of **A** is given by

$$\mathbf{A}=\mathbf{U}\sum\mathbf{V}^{\mathbf{H}} \quad (3)$$

where **Σ** is a diagonal matrix of singular values, and the left and right singular matrices **U** and **V** form orthogonal bases for the data space and object space, respectively. The TSVD is a rank limited, SVD-based inverse obtained by discarding a number of the least significant singular values and associated vectors. Written as a sum of left and right singular vectors $\mathbf{u}_i$ and $\mathbf{v}_i$ an estimate of the object is found from the data **b** as

$$\hat{\mathbf{x}}=\sum_{i=1}^{i_n}\left(\frac{\mathbf{u}_i^H\mathbf{b}}{\sigma_i}\right)\mathbf{v}_i \quad (4)$$

where i_n is the truncation index and σ_i is the ith singular value. The information available from the data is limited to the components supported by the span of the data-space basis formed by the left singular vectors, and the estimate of the object is limited to the components supported by the span of the object-space basis formed by the right singular vectors. Noise or errors in the data **b** are amplified by the inverse of the corresponding small singular values and mapped as spurious components of the object estimate. An optimal truncation index (with respect to noise and errors in **A** and **b**) can be found by maximizing the fidelity of the object estimate in (4) over the truncation index $i_n \in \{1, \ldots, N\}$. The maximum fidelity of $\hat{x}$ is related to the quality of the information in b, and the corresponding optimal truncation index is related to the quantity of information in **b**.

III. Methods

The general background of the previous section is now extended to the application of interest. Three-dimensional microwave breast imaging presents a large-scale, nonlinear inverse problem characterized by an ill-posed, under-determined scattering matrix. The nonlinearity of (1) arises from the dependence of the total field in the imaging region on the unknown dielectric profile of the object to be imaged. An approximation of the total field is often used to linearize the equations during solution the problem. However, for the purposes of this analysis we wish to evaluate the fundamental limits of microwave illumination in revealing information on the properties and structure of the unknown object. A computational electromagnetics technique is applied to the test domains (described in Section IV) to acquire simulated channel measurements of numerical breast phantoms. We further exploit the use of a full-wave field solver to compute Green's functions of the background media and to record the total fields in the imaging region with the object present. Green's function $\mathbf{G}^{\overline{b}}(\mathbf{r}_i, \mathbf{r}')$ at location $\mathbf{r}'$ in the imaging region is computed using the principle of reciprocity and the background fields $\boldsymbol{E}^b$ observed at $\mathbf{r}'$ when the ith probe location is sourced for each orthogonal polarization [27].

Green's functions may be computed for background models comprised of either homogeneous or heterogeneous media. Heterogeneous backgrounds may include known

boundary conditions, physical antenna models, or initial estimates of the boundary and properties of the unknown object. The total fields and Green's functions are used to construct a scattering matrix that is nearly exact, limited only by numerical precision, the accuracy of the electromagnetic solver, and the discretization of the integral equation. This exact formulation may be used as a benchmark in evaluating the linearizing approximations and initial conditions used in practical formulations. To further idealize the benchmark, we include an exact skin layer in the background model so that we can isolate the ability of the microwaves to image the finely detailed tissue structures of the breast interior. The interior breast volume is then filled with a homogeneous material with properties equal to the volume average of the breast phantom interior [15]. The scattering system is also analyzed in Section V without the use of this *a priori* information to evaluate the effect of the scattering response of the skin.

The cost of computing the SVD of the large-scale scattering matrix is prohibitive. The number of columns in **A** is equal to the number of unknowns incurred in the discretization of the imaging volume on a sufficiently fine grid such that it will not limit the image resolution achievable by the system. The number of rows is equal to the number of channel measurements, resulting in a highly under-determined system of equations. Noting that (2) is often solved using methods operating on the normal system of equations, we compute the eigendecomposition of the symmetric matrix $\mathbf{A}\mathbf{A}^H$

$$\hat{x}=\sum_{i=1}^{i_n}\left(\frac{\mathbf{w}_i^H\mathbf{b}}{\lambda_i}\right)\mathbf{A}^H\mathbf{w}_i \quad (5)$$

The fidelity of the estimates from aforementioned equation must be quantitatively evaluated so that an optimal truncation index i_n can be determined. Since the true object profile is readily available in the numerical test regime, the estimate $\hat{\mathbf{x}}$ is best judged in direct comparison to this exact solution $\mathbf{x}^*$. Although such comparisons are often made according to an error norm $\|\mathbf{x}^* - \hat{\mathbf{x}}\|$, we quantify the fidelity by correlating the estimate and the exact solution using a normalized inner product [15]

$$f(\hat{\mathbf{x}})=\frac{\langle \mathbf{x}*, \hat{\mathbf{x}}\rangle}{\|\mathbf{x}*\|_2\|\hat{\mathbf{x}}\|_2}. \quad (6)$$

We choose this scale-independent metric as it tends to demonstrate more sensitivity to truncation index than the error norm. Due to the large relative magnitude of the scattering from the skin layer and the associated imaging error, the metric is applied to a subregion of the imaging volume defined as the interior breast volume 6 mm away from the skin. These omissions are reasonable in the context of the application, as the skin layer is not an area of interest and the region beneath the skin is accessible to direct examination by palpation.

IV. Models

Investigating microwave imaging in the numerical regime offers two significant advantages: the availability of the total field over the imaging volume, and the ability to work with

highly realistic breast phantoms with knowledge of the exact distribution and properties of the tissues. We select one Class 2 numerical breast phantom ("scattered fibroglandular," ID number 010204) and one Class 3 numerical breast phantom ("heterogeneously dense," ID number 062204) from the University of Wisconsin repository [25].

The dielectric properties of the dispersive media to be used in the numerical phantoms are obtained by fitting measured data to Debye models. The breast tissue properties are based on data published by Lazebnik *et al.* [2], the properties of the skin layer are based on data published by Gabriel *et al.* [28], and the properties of the immersion medium are based on experimental measurements of safflower oil [29]. The measured frequency-dependent complex permittivities of each material are fitted by single-pole Debye models over a frequency range of 0.5–3.5 GHz. The complex permittivity is given parametrically as follows, where ε_s is the static permittivity, ε_∞ is the infinite permittivity, σ_s is the static conductivity, and τ is the time constant of the relaxation pole

$$\varepsilon_c(\omega, \varepsilon_s, \varepsilon_\infty, \sigma_s, \tau) = \varepsilon_\infty + \frac{\varepsilon_s - \varepsilon_\infty}{1 + j\omega\tau} + \frac{\sigma_s}{j\omega\varepsilon_0}. \quad (7)$$

The resulting model parameters are listed in Table I. Due to practical considerations of the electromagnetic simulations, the time constant is fixed to 15 ps for all materials. The numerical breast phantoms are mapped from MRI data as described in [26] using the Debye models of Table I. The grid resolution is 0.5 mm and the domains are cropped to accommodate a cylindrical antenna array and to remove the chest wall from the models. The homogeneous skin is given a 2.0-mm thickness.

Simulated field measurements are acquired using the FDTD method. Forty source and observation points are distributed over a cylindrical surface sized to fit the breast phantoms with a minimum of 1-cm spacing to the skin surface. Locations are chosen every 45° on each of five coronal rings, with the rings equally spaced along the axial extent of the breast phantom. The second and fourth rings are rotated by 22.5° to increase the element spacing between adjacent rings. The distance between adjacent array element locations is about 16 ± 2 mm for both phantoms. Soft current sources with no physical antenna allow sourcing and receiving of all three Cartesian polarizations. An appropriately weighted vector sum then achieves arbitrarily directed source and receive polarizations. The *z*-directed vertical polarizations at the array locations are illustrated in Fig. 1. Horizontal polarizations at each location are simulated by sum of the *x* and *y* field components, weighted such that the polarization is oriented along the horizontal tangent of the cylindrical array surface. Since the FDTD field components are arranged on a staggered grid, *x*, *y*, or *z* field components are sourced or observed on both sides of a given point such that the three source polarizations share a common phase center. Eight electric field components are soft-sourced with the same pulse function, giving a constant current distribution with a 4.0-mm length and a 0.5 mm × 0.5 mm cross section. Although the low radiation efficiency of the electrically small sources results in measurement amplitudes averaging about −80 dB relative to the source magnitude, the computational noise floor of the single-precision FDTD simulations is about −140 dB.

An individual FDTD simulation is run for each source location and each source polarization, with a modulated Gaussian excitation pulse of sufficient bandwidth to cover the frequency range of interest. Electric field measurements are recorded for each polarization through each unique spatial channel. Data are recorded as the electric field averaged over the eight field components centered on the observation point, for each of the *x*, *y*, and *z* polarizations. The vector electric field is recorded for each case over the imaging volume on a downsampled grid of 2.0-mm resolution. The time domain data are transformed to the frequency domain at 0.5, 1.0, 1.5, 2.0, and 2.5 GHz, and the resulting phasor data are normalized by the frequency response of the electric field source pulse.

V. Results

The analysis described in Section III is applied to field data collected from the numerical breast phantoms defined in Section IV. We analyze both single-frequency and multiple-frequency formulations of (1), with the unknown contrast expressed in terms of complex permittivity, $\varepsilon_c = k^2/\omega^2\mu_0$, rather than the square of the wavenumber. In the single frequency case, the unknown elements of x are complex permittivity contrasts of the form $(\varepsilon_c^* - \hat{\varepsilon}_c)$. In the multiple-frequency formulation, the dispersive, frequency-dependent complex permittivity is posed by the real-valued unknown parameters of the single-pole Debye model [23]. In addition, we investigate the use of the analysis in the selection of channels and in the formulation of the inverse problem. The method is further employed to evaluate the effect of noise in the data, modeling errors, and field approximations.

A. Single-Frequency Formulation

Systems of single-frequency scattering equations at 0.5, 1.0, 1.5, 2.0, and 2.5 GHz are constructed for analysis using fields from the Class 3 phantom test bed. The systems are formulated with phasor data from vertically polarized channels and the scattering matrices are constructed using tensor Green's functions and vector total fields corresponding to the vertical source and receive polarizations. Each system consists of 820 equations corresponding to 780 bistatic channel measurements and 40 monostatic channel measurements. The unknowns are the complex-valued permittivity contrasts over the N voxels in the imaging region V, which is restricted to the volume interior to the skin layer. On the 2-mm grid, the Class 3 phantom interior contains about 42 000 voxels. The fidelity is computed by applying (6) to a subset of the the $N \times 1$ elements of the exact and estimated contrast vectors, as described in Section III.

Fig. 2 charts the fidelity of the TSVD image as the truncation level and signal-to-noise ratio (SNR) are varied for each operating frequency. An improvement in the peak fidelity is evident in Fig. 2(a) at the higher frequencies. The optimal truncation index corresponding to peak fidelity increases with frequency. The optimal truncation index provides a measure of the effective rank of the system. The noise performance of a system may be illustrated by examining the peak fidelity of the TSVD estimate as a function of SNR (where 0 dB is the source level). Fig. 2(b) shows the effect on peak fidelity of additive white noise in the data for single-frequency formulations. The curves illustrate the required measurement sensitivity at a given frequency. Note the competing considerations of higher losses at higher frequencies versus lower radiation efficiency at lower frequency (due to the fixed physical

source length). More efficient antennas or higher loss media (e.g., larger or denser breasts) would translate these curves to the left and right, respectively.

The spatial frequency content of the singular vectors generally increases with singular-value index [21]; thus, the increase in optimal truncation index with frequency demonstrated by Fig. 2(a) suggests that the resolution of the resulting images will improve as frequency increases. The trend in image resolution with frequency is visualized adding the TSVD-estimated contrast vector $\hat{x}$ to the background and viewing the result over the 3-D imaging volume. Coronal cross sections of the imaging volume at each frequency are represented in Fig. 3. The corresponding cross section of the exact phantom profile is shown for comparison in Fig. 3(a).

In addition to the comparison across frequencies, we investigate the information held by single-frequency scattering data with respect to the relative permittivity and effective conductivity parameters. The fidelity of each parameter is computed by applying (6) separately to the real and imaginary parts of the exact and estimated complex permittivity contrasts. Fig. 4 clearly indicates that the effective conductivity is more poorly estimated than the relative permittivity throughout the UHF band.

B. Multiple-Frequency Formulation

The TSVD analysis can be used to inform the choice of a particular formulation of the problem to be inverted. For example, simultaneous multiple-frequency solutions can be compared to single-frequency formulations and comparisons can be made of various choices of assumed frequency dependence for the unknown dielectric properties. Over the UHF band the single-pole Debye model is a natural choice for constraining the frequency dependence of biological tissues, whose responses are dominated by their water content and the single-pole behavior of water in the band. With the time-constant of the pole fixed for all tissues, the unknowns are formulated as the three remaining free parameters of the Debye model: static permittivity ε_s, infinite permittivity ε_∞, and static conductivity σ_s. The Debye model is alternatively expressed with the static permittivity parameter replaced by a parameter $\Delta\varepsilon = \varepsilon_s - \varepsilon_\infty$, which corresponds directly to the dispersive term in the Debye relation (7). We have included all three Debye permittivity parameters in this analysis for completeness, though since they collectively represent 2 DOF only $\Delta\varepsilon$ and ε_∞ are estimated.

A multiple-frequency scattering system is constructed using field data at 0.5, 1.0, 1.5, 2.0, and 2.5 GHz from the Class 3 phantom test bed. The formulation uses vertically polarized channel data and the scattering matrices are computed using tensor Green's functions and vector total fields corresponding to the vertical source and receive polarizations. The system comprises 8200 equations consisting of the real and imaginary equation pairs for each of 820 channels at each of the five frequencies. The $3N \times 1$ vector x is the concatenation of three $N \times 1$ vectors of the real-valued Debye parameters. The construction of the linear system of equations in the Debye parameter unknowns is described in detail elsewhere [27].

As in the single-frequency cases earlier, the imaging region is restricted to the volume interior to the skin layer. Fig. 5 shows coronal cross sections of the actual and estimated interiors of the Class 2 and Class 3 phantoms. The fidelity is computed by applying (6) to

the $3N \times 1$ vectors of exact and estimated Debye parameter contrasts. Fig. 6 shows the fidelity versus SNR of each parameter of the optimal TSVD solution to the five-frequency Debye formulation of the inverse problem. Similar to the single-frequency results in Fig. 4, the static conductivity parameter of the multiple-frequency Debye formulation is shown to be poorly estimated by the scattering data compared to the estimation performance for the permittivity parameters. It is important to note that the scattering equations at each frequency in the multiple-frequency formulation are inherently weighted by the frequency-dependent radiation efficiency of the source. Artificial weighting of the the scattering equations by frequency is another interesting candidate for the TSVD analysis.

C. System Design

The selection of a set of measurement channels for an imaging system is a significant design consideration. A channel is defined by the locations of the source and receiver, the polarizations of the source and receiver, and the frequency of the source. The selection of frequency is investigated earlier; here we compare the information for varied selections of polarization and spatial channels.

The effect of the polarization on the information content of the scattering data can be studied by sourcing and observing the field components corresponding to the polarizations of interest. Any combination of co- and cross-polarization channels can be analyzed in this way. For illustration, we compare vertical source and receive polarization to horizontal source and receive polarization. For the cylindrical array of source-receive locations described in Section IV, the $\boldsymbol{E}_z$ field component is defined as the vertical polarization. The horizontally polarized illumination and observation are achieved by proportionally combining the *x*- and *y*-directed field components as described in Section IV. For each case of polarization, the multiple-frequency formulation is constructed using data at 0.5, 1.0, 1.5, 2.0, and 2.5 GHz from all 820 spatial channels. The fidelity of the static permittivity estimate for each polarization versus SNR is shown in Fig. 7. The performance of the polarizations is similar, indicating that there is comparable imaging information available from either vertically or horizontally copolarized scattering data.

The spatial selection of channels requires consideration of the array shape and the population density of elements in the array. In addition, it is of interest to consider whether certain channels contain better or different information than others. We investigate one example of channel selection by distinguishing between *through* and *reflect* channels. In the cylindrical array configuration with the origin on the cylindrical axis, we define the *through* channels as the channels in which the receive location is equal to or greater than 90° from the source location, and the *reflect* channels are defined as the channels in which the receive location is equal to or less than 90° from the source location. For the 40-element array described in Section IV, there are 556 through channels and 556 reflect channels. The fidelity versus truncation index of each channel set is charted in Fig. 8(a) for the $3N \times 1$ contrast estimates of the multiple-frequency Debye parameter formulation. Although the peak fidelity is about equal each case, the difference in the optimal truncation indices suggest that through channel data favor lower spatial frequency solutions while reflect channel data favor higher spatial frequency solutions. This result is consistent with the

Fourier-space treatment of microwave imaging in [16] and [30] where it is shown for linear arrays of sources and receivers that the through data captures lower spatial frequencies and the reflect data captures higher spatial frequencies. Cross sections of the through and reflect image estimates in Fig. 8(b) and (c) illustrate the difference in resolution. Comparison to the exact cross section in Fig. 5 suggests that the information content of each is complementary and that both should be used.

D. Error Evaluation

The preceding results have shown the use of the TSVD analysis for noise errors in the data. Others sources of errors in the data vector or in the scattering matrix can be analyzed in a similar manner. We illustrate the evaluation of such errors with a few representative examples. The performance of the scalar-field approximation is investigated, imperfect estimation of the skin layer is visualized, and the Born approximation of the total field is evaluated.

The scalar field approximation is a computationally advantageous simplification of the inverse problem formulation that introduces an error in the scattering matrix. The validity of the scalar field approximation, in which Green's functions and total fields calculated in the imaging region are assumed to be scalar, is compared to the exact formulation in which the tensor Green's functions and vector total fields are used. In our scalar example, only the *z*-component of the electric field and the *zz*-component of Green's functions are used in the construction of the scattering matrix. For vertical source and observation polarizations, 820 spatial channels at each of five frequencies are used to evaluate the fidelity of the complex permittivity estimate versus truncation index for the scalar and vector scattering matrix formulations for the Class 3 phantom. Fig. 9 shows the limitation of the scalar-field-approximated scattering matrix in mapping the information available from multiple-frequency data.

The results in Section V-A– C used the simplifying assumption that the skin region is exactly modeled in the background media, allowing us to isolate the performance of a microwave system in imaging the detailed heterogeneous tissue distributions of the breast interior. We can compare this to the performance of the system with no *a priori* information by using a homogeneous background of the immersion medium. The imaging volume is defined to extend 6 mm away from the outer skin surface. The optimal TSVD images of multiple-frequency data at 0.5, 1.0, 1.5, 2.0, and 2.5 GHz with and without the background skin model are shown in Fig. 10(b) and (c). In the cross section shown in Fig. 10(c) the skin layer is only partially reconstructed by the data. Although any residual scattering from an imperfect estimation of the skin layer will manifest as clutter elsewhere in the imaging region, Fig. 10(a) shows that the fidelity and rank of the estimate are actually higher than that of the formulation using *a priori* background information. The higher optimal truncation index suggests increased resolution, which is supported by a visual comparison of the images. Higher spatial frequencies are likely emphasized in the solution due to the presence of the data of the scattering from the thin, high contrast skin layer.

The analyses presented in this paper exploit the availability of the exact total field over the entire unknown imaging region in order to evaluate the ability of the microwave scattering

data to image the breast. In practice, the total field term $\boldsymbol{E}^t$ in the scattering relation of (1) is unknown and dependent on the unknown contrast. Solutions to the inverse scattering problem must, therefore, approximate the total field term. The Born approximation [4] is commonly used, in which the total field is replaced the by incident field in the background region. The Born approximation is known to be inaccurate for electrically large objects with high contrast relative to the background, which is certainly the case for the breast volume. The error due to the use of the Born approximation in the microwave breast imaging application can be evaluated by the TSVD analysis. A multiple-frequency scattering matrix is formulated with the exact total fields replaced by the fields measured in the *a priori* background. The effect of the Born approximation on the image fidelity is demonstrated in Fig. 11 for the static permittivity and static conductivity Debye parameters. The system is formulated using data from 820 channels at 0.5, 1.0, 1.5, 2.0, and 2.5 GHz. The comparison underscores the limited utilization of the information in the data when the Born approximation is employed. Iterative methods of nonlinear optimization such as the Born iterative and distorted-Born iterative methods are often used to overcome this limitation. In the context of such methods, Fig. 11 gives an expectation of performance for the first iteration. The performance of the conductivity estimation is so low in the Born approximation that it suggests the use of an iterative technique that favors permittivity solutions in early iterations. The lower optimal truncation index of the Born approximation formulation suggests that low-pass regularization should be increased during early iterations.

VI. Discussion

The single-frequency performance relative to the singular-value truncation index in Fig. 2(a) shows that as frequency is lowered, fewer and fewer of the singular basis vectors corresponding to the higher indices are informed by the data. Since the spatial frequencies of the singular vectors generally increases with singular-value index, this trend suggests that low-frequency formulations should be increasingly regularized by low-pass filtering to avoid noise components in the part of the singular spectrum for which the data have no information. Furthermore, this trend may suggest that a frequency-hopping method of imaging may be effective, in which the solution for each frequency of operation is filtered accordingly. The measurement sensitivity required for a given system to image experimental or clinical data can be estimated by analysis of numerical data over SNR such as in Figs. 2(b) and 6. The results of Figs. 4 and 6(a) reveal that the conductivity properties of the unknown objects are more poorly estimated from the scattering data than the permittivity properties. Given the rough correlation between the permittivity and conductivity properties of biological tissues, a higher fidelity estimate of the conductivity might be obtained indirectly from the permittivity estimate rather than by direct estimation from the data.

One goal of the method presented in this paper is to provide a loose sense of an upper bound on imaging performance that can be expected from a given microwave breast imaging system under ideal conditions. However, when speaking of upper bounds on imaging performance, it is important to clarify that the TSVD analysis optimizes the fidelity metric over the l_2 norm. Cost functions and regularizations based on the this norm are known to have a low-pass filtering effect on the spatial frequencies of the solution. The TSVD is itself a method of inversion and regularization, with an effect similar to the Tikhonov method of

regularization [21]. Alternative formulations and techniques of inversion and regularization intended to improve resolution and edge preservation have been investigated elsewhere and have potential to out-perform results illustrated by TSVD analysis. However, all approaches are fundamentally limited with respect to the information available from the data. The TSVD analysis is adept at the comparative evaluation of that information. It is, therefore, a powerful tool for the design of the measurement system and the formulation of the inverse problem, irrespective of the eventual choice of imaging technique used to recover the unknown object.

There are a number of idealizations employed by our analysis in service of the goal of evaluating imaging performance. Practical performance expectations are tempered by some of these idealizations. The exact total fields in the imaging region are available in a computational study, but in practice they must be estimated as discussed in the analysis of the Born approximation in Section V-D. The Hertzian current sources simplify polarization analysis, but exhibit none of the mutual coupling or modeling errors arising with the use of actual antennas. The inclusion of the exact skin model in the background allows us to isolate the ability of the microwaves to resolve realistic tissue structures in the breast interior, but the skin tissue presents a scattering response that is quite large compared to interior scattering, and therefore, small errors in the modeling or imaging of the skin layer may result in significant image distortion. Although idealizations such as these may be seen as overly contrived from a practical perspective, the effect of each idealization and source of error can be analyzed by the TSVD analysis and their cost on performance can be objectively quantified. In addition, the idealized images may provide a useful benchmark for practical imaging results than comparison to the exact profile of the numerical phantoms.

Many important issues in microwave imaging design are not included in this investigation, but most can be analyzed in a similar manner. For example, the shape and population of the antenna array can be optimized using the TSVD analysis. The properties of the immersion medium have significant implications on antenna and array design and impacts the coupling of illumination into the breast interior. The TSVD analysis can be used to evaluate the imaging performance for various selections of immersion media. Although inverse scattering techniques for breast imaging typically operate at frequencies in the UHF band (300 MHz to 3 GHz), tissue-penetrating radar techniques (e.g., [31] and [32]) are often designed in the UWB band (3.1 to 10.6 GHz). Since both methods are based on the same scattering phenomena it is a natural extension of the TSVD analysis to consider the usable information content of data in the UWB band, particularly with respect to measurement sensitivity. These and many other considerations in system design and problem formulation are readily analyzed by the techniques employed herein.

VII. Conclusion

A method of analysis using the TSVD has been presented in which the scattering data may be systematically evaluated independently from the development of imaging methods to be applied to the data. The method was used to compare the information available from the data for frequencies in the UHF band, for single- and multiple-frequency formulations, for different selections of measurement channel locations, and for errors due to measurement

noise and field approximations. The results can be used to evaluate the tradeoff between field penetration and image resolution over frequency and to inform the practical measurement sensitivity necessary to utilize the data at each frequency. Limitations in data utilization were shown when using the scalar field approximation or Born approximation in the formulation of the breast imaging problem. In addition to the considerations investigated in this paper, the TSVD analysis of scattering data and inverse formulation can be used to systematically optimize and evaluate a microwave imaging system, from the design of the test fixture to the analysis of noise and modeling errors. Any microwave breast imaging method stands to benefit from the betterment of the information in the data available from a system developed in this manner.

Acknowledgments

This work was supported by the National Institutes of Health under grant R01 CA112398 awarded by the National Cancer Institute, and the Philip D. Reed chaired professorship.

References

1. Fear EC, Hagness SC, Meaney PM, Okoniewski M, Stuchly MA. Enhancing breast tumor detection with near-field imaging. IEEE Microw Mag. Mar; 2002 3(1):48–56.
2. Lazebnik M, McCartney L, Popovic D, Watkins CB, Lindstrom MJ, Harter J, Sewall S, Magliocco A, Booske JH, Okoniewski M, Hagness SC. A large-scale study of the ultrawideband microwave dielectric properties of normal breast tissue obtained from reduction surgeries. Phys Med Biol. 2007; 52:2637–2656. [PubMed: 17473342]
3. Lazebnik M, Popovic D, McCartney L, Watkins CB, Lindstrom MJ, Harter J, Sewall S, Ogilvie T, Magliocco A, Breslin TM, Temple W, Mew D, Booske JH, Okoniewski M, Hagness SC. A large-scale study of the ultrawideband microwave dielectric properties of normal, benign, and malignant breast tissues obtained from cancer surgeries. Phys Med Biol. 2007; 52:6093–6115. [PubMed: 17921574]
4. Chew, WC. Waves and Fields in Inhomogeneous Media. Piscataway, NJ: IEEE Press; 1995.
5. van den Berg PM, Kleinman RE. A total variation enhanced modified gradient algorithm for profile reconstruction. Inverse Probl. 1995; 11(3):LS–L10.
6. Abubakar A, van den Berg PM, Mallorqui JJ. Imaging of biomedical data using a multiplicative regularized contrast source inversion method. IEEE Trans Microw Theory Tech. Jul.2002 50(7): 1761–1771.
7. Mojabi P, LoVetri J. Overview and classification of some regularization techniques for the Gauss-Newton inversion method applied to inverse scattering problems. IEEE Trans Antennas Propag. Sep.2009 57(9):2658–2665.
8. Mojabi P, LoVetri J. Enhancement of the Krylov subspace regularization for microwave biomedical imaging. IEEE Trans Med Imag. Dec.2009 28(12):2015–2019.
9. Irishina N, Alvarez D, Dorn O, Moscoso M. Structural level set inversion for microwave breast screening. Inverse Probl. Mar.2010 26(3):035015.
10. Semenov S, Bulyshev A, Abubakar A, Posukh V, Sizov Y, Souvorov A, van den Berg P, Williams T. Microwave-tomographic imaging of the high dielectric-contrast objects using different image-reconstruction approaches. IEEE Trans Microw Theory Tech. Jul.2005 53(7):2284–2294.
11. Abubakar A, Hu W, van den Berg PM, Habashy TM. A finite-difference contrast source inversion method. Inverse Probl. 2008; 24(6):065004-1–065004-17.
12. Rubæk T, Kim O, Meincke P. Computational validation of a 3-D microwave imaging system for breast-cancer screening. IEEE Trans Antennas Propag. Jul.2009 57(7):2105–2115.
13. Gilmore C, Mojabi P, LoVetri J. Comparison of an enhanced distorted Born iterative method and the multiplicative-regularized contrast source inversion method. IEEE Trans Antennas Propag. Aug.2009 57(8):2341–2351.

14. Fang Q, Meaney P, Paulsen K. Viable three-dimensional medical microwave tomography: Theory and numerical experiments. IEEE Trans Antennas Propag. Feb.2010 58(2):449–458. [PubMed: 20352084]
15. Shea JD, Kosmas P, Hagness SC, Van Veen BD. Three-dimensional microwave imaging of realistic numerical breast phantoms via a multiple-frequency inverse scattering technique. Med Phys. Aug.2010 37(8):4210–4226. [PubMed: 20879582]
16. Slaney M, Kak A, Larsen L. Limitations of imaging with first-order diffraction tomography. IEEE Trans Microw Theory Tech. Aug.1984 32(8):860–874.
17. Bucci O, Franceschetti G. On the spatial bandwidth of scattered fields. IEEE Trans Antennas Propag. Dec.1987 35(12):1445–1455.
18. Bucci O, Franceschetti G. On the degrees of freedom of scattered fields. IEEE Trans Antennas Propag. Jul.1989 37(7):918–929.
19. Bucci O, Isernia T. Electromagnetic inverse scattering: Retrievable information and measurement strategies. Radio Sci. Nov-Dec;1997 32(6):2123–2137.
20. Hori M. Inverse analysis method using spectral decomposition of Green's function. Geophys J Int. Oct.2001 147(1):77–87.
21. Hansen, PC. Rank-Deficient and Discrete Ill-Posed Problems: Numerical Aspects of Linear Inversion. Philadelphia, PA: SIAM; 1998.
22. Fang Q, Meaney PM, Paulsen KD. Singular value analysis of the Jacobian matrix in microwave image reconstruction. IEEE Trans Antennas Propag. Aug.2006 54(8):2371–2380.
23. Winters DW, Shea JD, Kosmas P, Veen BDV, Hagness SC. Three-dimensional microwave breast imaging: Dispersive dielectric properties estimation using patient-specific basis functions. IEEE Trans Med Imag. Jul.2009 28(7):969–981.
24. Crocco L, Litman A. On embedded microwave imaging systems: Retrievable information and design guidelines. Inverse Probl. 2009; 25(6):065001.
25. UWCEM Numerical Breast Phantom Repository. University of Wisconsin Computational Electromagnetics Laboratory; [Online]. Available: http://uwcem.ece.wisc.edu
26. Zastrow E, Davis SK, Lazebnik M, Kelcz F, Van Veen BD, Hagness SC. Development of anatomically realistic numerical breast phantoms with accurate dielectric properties for modeling microwave interactions with the human breast. IEEE Trans Biomed Eng. Dec.2008 55(12):2792–2800. [PubMed: 19126460]
27. Shea JD, Kosmas P, Van Veen BD, Hagness SC. Contrast-enhanced microwave imaging of breast tumors: A computational study using 3D realistic numerical phantoms. Inverse Probl. Jul.2010 26(7):074009.
28. Gabriel S, Lau RW, Gabriel C. The dielectric properties of biological tissues: III. Parametric models for the dielectric spectrum of tissues. Phys Med Biol. 1996; 41:2271–2293. [PubMed: 8938026]
29. Al-Joumayly NBMA, Aguilar SM, Hagness SC. Dual-band miniaturized patch antennas for microwave breast imaging. IEEE Antennas Wireless Propag Lett. 2010; 9:268–271.
30. Larsen, LE.; Jacobi, JH. Microwave imaging with first order diffraction tomography. In: Larsen, LE.; Jacobi, JH., editors. Medical Applications of Microwave Imaging. 1986. p. 184-212.
31. Li X, Davis SK, Hagness SC, van der Weide D, Veen BDV. Microwave imaging via space-time beamforming: Experimental investigation of tumor detection in multi-layer breast phantoms. IEEE Trans Microw Theory Tech. Aug.2004 52(8):1856–1865.
32. Sill JM, Fear EC. Tissue sensing adaptive radar for breast cancer detection—Experimental investigation of simple tumor models. IEEE Trans Microw Theory Tech. Nov.2005 53(11):3312–3319.

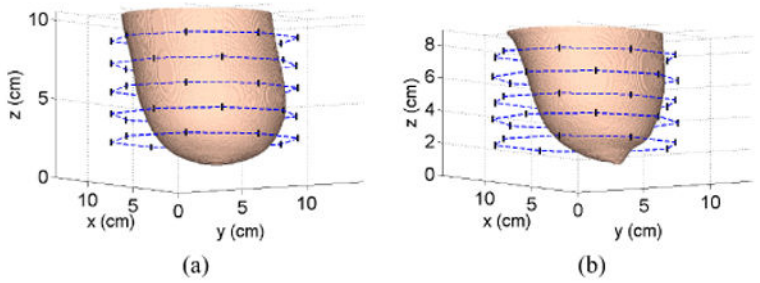

Fig. 1.

(a) Class 2 and (b) Class 3 breast phantoms with array locations shown by vertically polarized (*z*-directed) 4-mm sources.

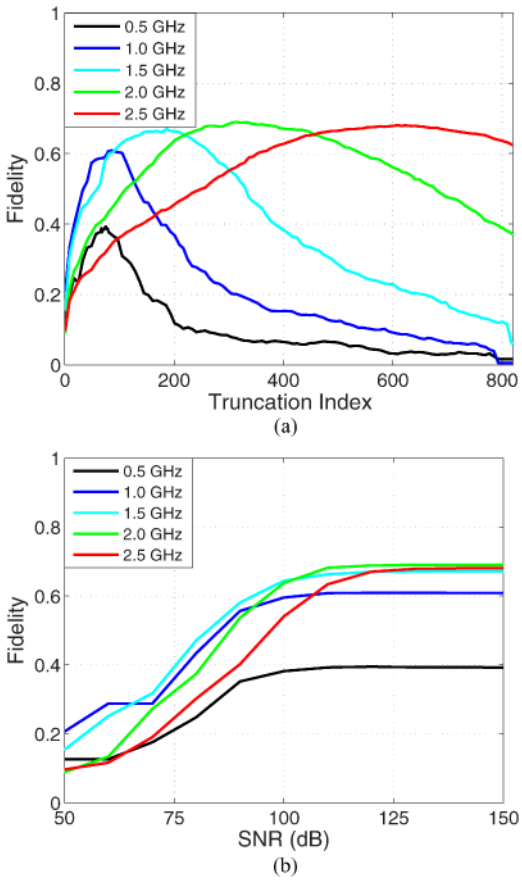

Fig. 2.

Fidelity of TSVD estimates of complex permittivity using single-frequency data from 820 measurement channels of the Class 3 phantom. (a) Fidelity versus truncation index. (b) Peak fidelity versus SNR.

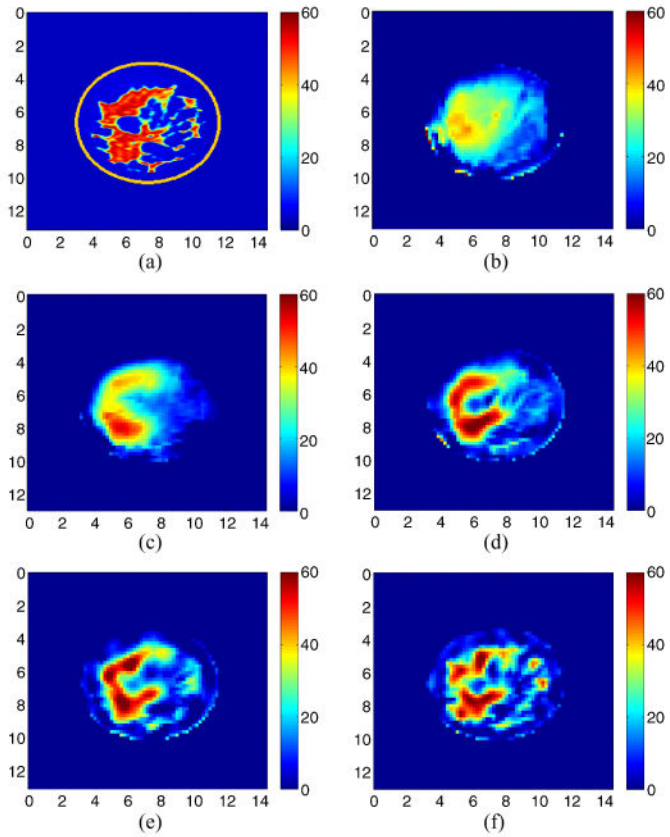

Fig. 3.

Coronal cross sections of static permittivity ε_s for (a) Class 3 breast phantom, and for the optimal TSVD projections of the scattering data at (b) 0.5, (c) 1.0, (d) 1.5, (e) 2.0, and (f) 2.5 GHz. Axes in cm.

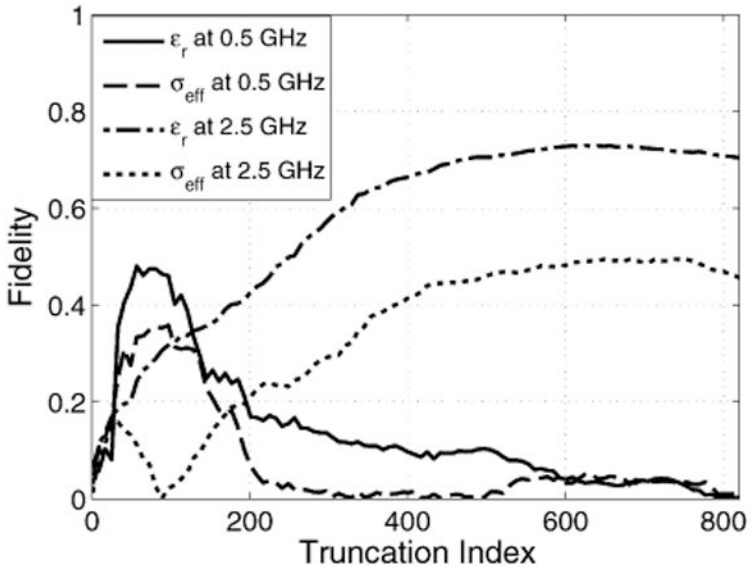

Fig. 4.

Fidelity versus truncation index of the TSVD estimates of relative permittivity ε_r and effective conductivity σ_{eff} at low and high frequency.

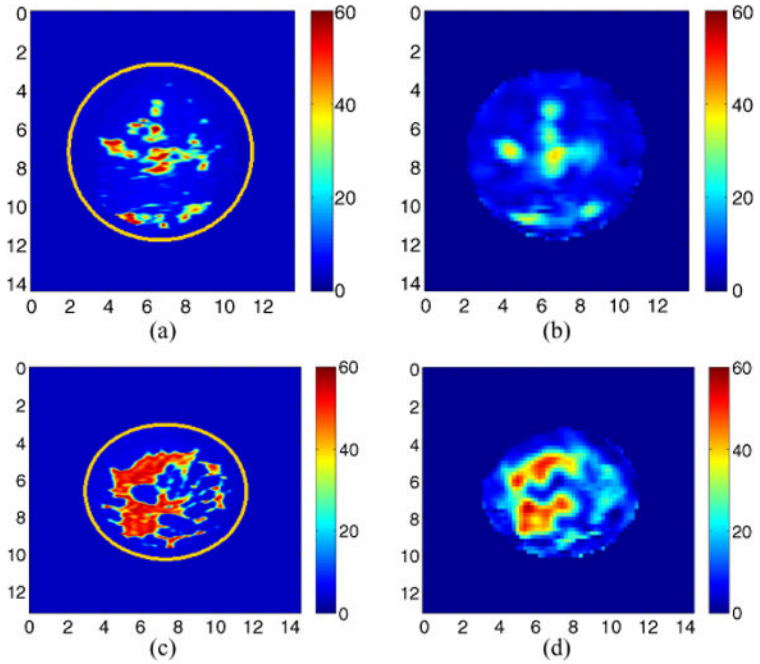

Fig. 5.

Coronal bisections of the exact phantom distributions and TSVD estimates of the static permittivity ε_s using multiple-frequency data at 0.5, 1.0, 1.5, 2.0, and 2.5 GHz. (a) Exact Class 2 phantom, (b) Class 2 estimate, (c) exact Class 3 phantom, (d) Class 3 estimate. Axes in cm.

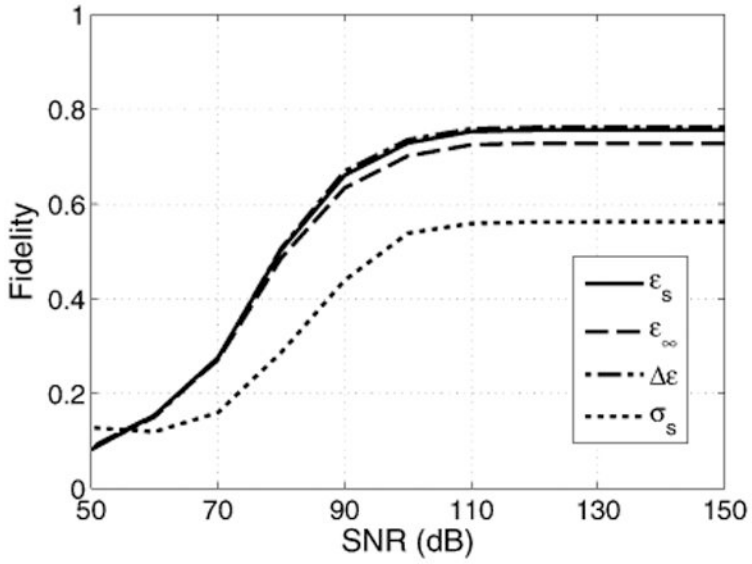

Fig. 6.

Peak fidelity versus SNR of TSVD-estimated Debye parameters for the Class 3 phantom using multiple-frequency data at 0.5, 1.0, 1.5, 2.0, and 2.5 GHz over 820 measurement channels.

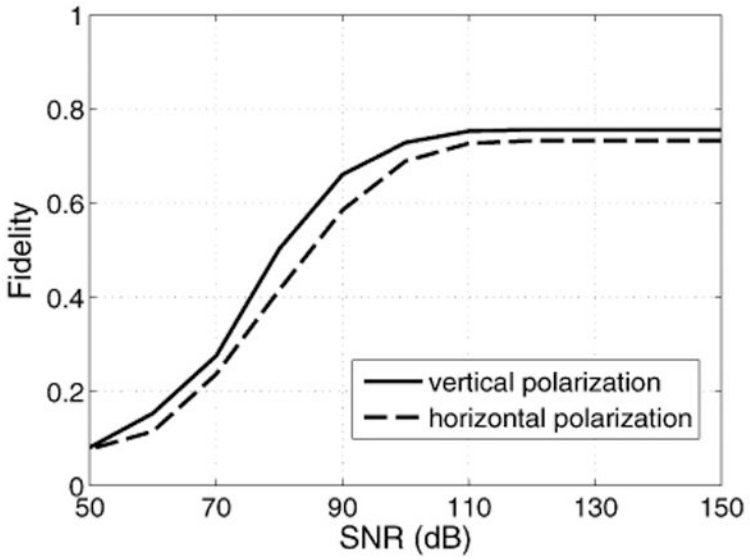

Fig. 7.

Peak fidelity of the static permittivity parameter versus SNR for vertical and horizontal polarizations. The TSVD estimates are computed from multiple-frequency data at 0.5, 1.0, 1.5, 2.0, and 2.5 GHz.

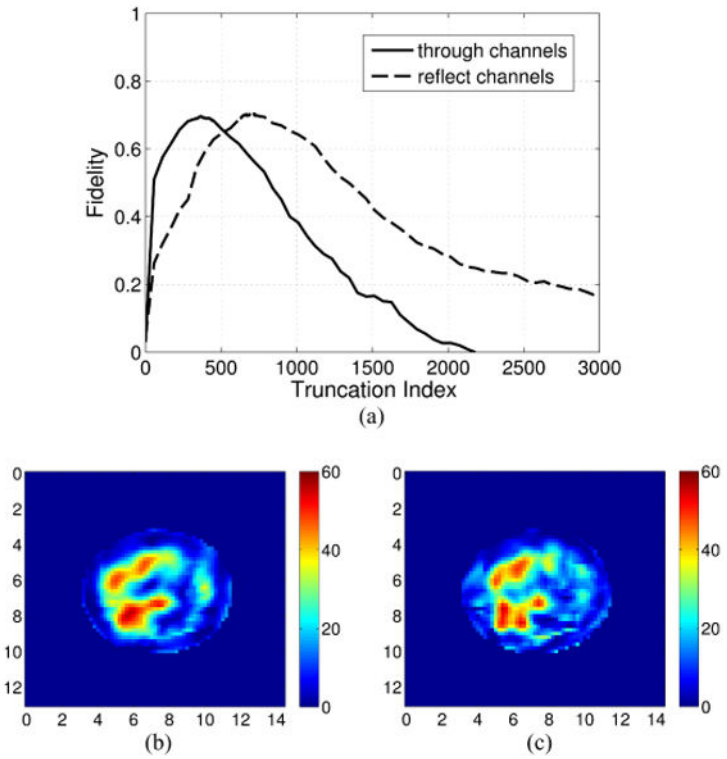

Fig. 8.

Comparison of “through” and “reflect” channels using a multiple-frequency Debye formulation with data at 0.5, 1.0, 1.5, 2.0, and 2.5 GHz. (a) Fidelity of the parametric Debye estimate versus truncation index. Coronal cross sections of the TSVD projections at the optimal truncation indices are shown for (b) through channels and (c) reflect channels. Axes in cm.

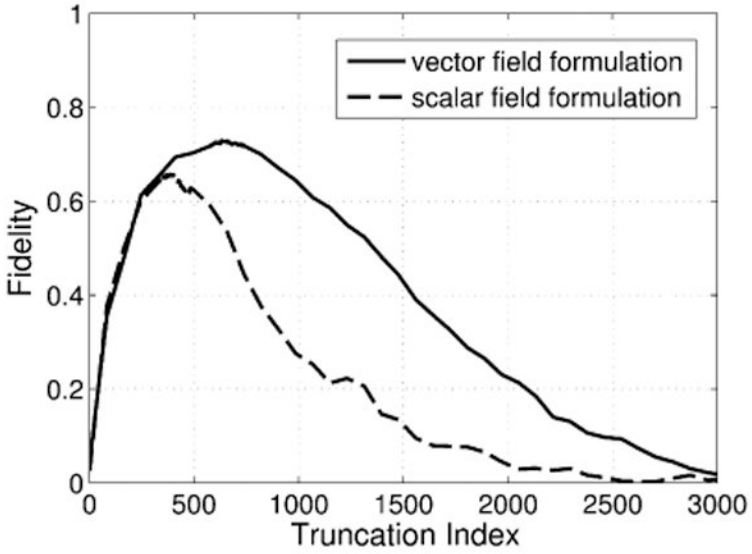

Fig. 9.

Comparison of the fidelity versus truncation index using the exact vector-field formulation and the approximate scalar-field formulation. Results are obtained from Class 3 phantom data at 0.5, 1.0, 1.5, 2.0, and 2.5 GHz.

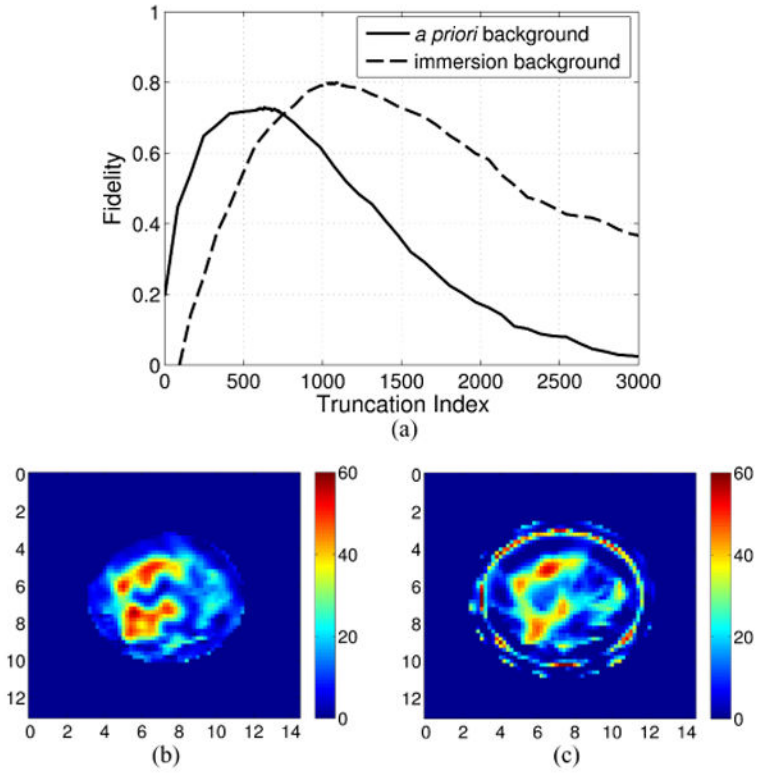

Fig. 10.

Effect of *a priori* background information using a multiple-frequency Debye formulation with data at 0.5, 1.0, 1.5, 2.0, and 2.5 GHz. The Class 3 phantom is analyzed with and without the exact skin model and volume-averaged interior properties included in the background. (a) Fidelity of the optimal TSVD estimates versus truncation index. Coronal cross sections of the optimal TSVD projections for (b) *a priori* and (c) immersion backgrounds. Axes in cm.

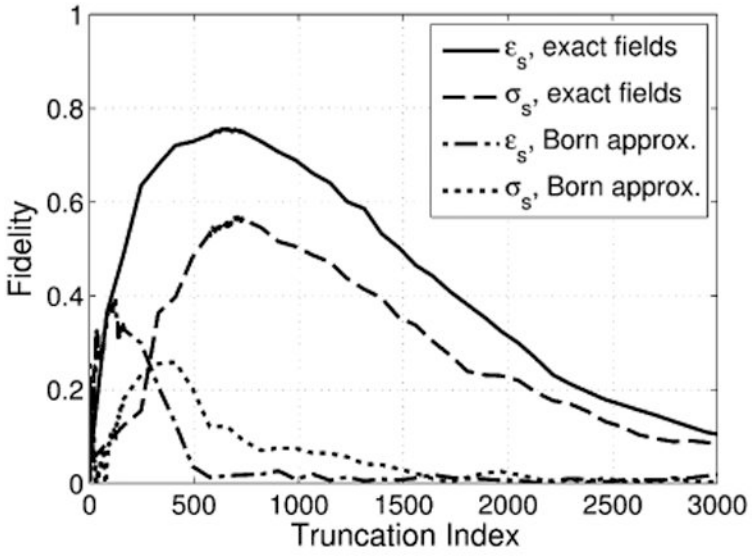

Fig. 11.

Fidelity of the ε_s and σ_s estimates versus truncation index with and without the Born field approximation for multiple-frequency data at 0.5, 1.0, 1.5, 2.0, and 2.5 GHz.

Table I

Debye Parameters (Static and Infinite Relative Permittivity ε_s and ε_∞ and Static Conductivity σ_s) of the Media Modeled in the Numerical Breast Phantoms

Material (percentile)	ε_s	ε_∞	σ_s (S/m)
Safflower oil	2.93	2.21	0.0120
Adipose tissue (min)	2.42	2.28	0.0023
Adipose tissue (25th)	4.07	2.74	0.0207
Adipose tissue (50th)	4.81	3.11	0.0367
Adipose tissue (75th)	7.62	4.09	0.0842
Fibroglandular tissue (25th)	36.7	16.8	0.461
Fibroglandular tissue (50th)	49.1	17.5	0.720
Fibroglandular tissue (75th)	54.3	18.6	0.817
Fibroglandular tissue (max)	67.2	29.1	1.38
Skin layer	40.1	15.3	0.741